ACS APPLIED NANO MATERIALS

www.acsanm.org Article

MnO Nanoparticles Embedded in Functional Polymers as T_1 Contrast Agents for Magnetic Resonance Imaging

Michele Mauri,[†] Veronica Collico,[†] Lucia Morelli,[†] Pradip Das, Isabel García, Jesus Penaranda Avila, Michela Bellini, Rany Rotem, Marta Truffi, Fabio Corsi, Roberto Simonutti, Luis M. Liz-Marzán, Miriam Colombo,* and Davide Prosperi

Cite This: *ACS Appl. Nano Mater.* 2020, 3, 3787−3797 Read Online

ACCESS | Metrics & More | Article Recommendations | Supporting Information

ABSTRACT: The design and development of contrast agents (CAs) for magnetic resonance imaging (MRI) in clinical analysis is expected to improve the image spatial resolution and to increase the detection sensitivity, especially regarding neurological disorders and cancer disease. In particular, advanced CAs for T_1-weighted images are investigated to achieve the sensitive detection of early-stage primary tumors or brain metastases. In this study, we present a strategy toward diagnostic T_1 CAs for MRI, based on polymer-modified MnO nanoparticles (NPs). Two different nanosystems were synthesized, consisting of (1) colloidal MnO nanocrystals wrapped by a multidentate amphiphilic polymer and (2) MnO nanocrystals embedded within poly(lactic-*co*-glycolic acid) (PLGA) NPs. These nanosystems were compared in terms of their MRI contrast power and biological safety. The latter system combines the excellent biocompatibility of PLGA with the unique magnetic properties of MnO NPs and allows sustained contrast enhancement over time. Longitudinal relaxivities of both MnO composite nanomaterials proved to be higher than those of commercial Gd-based CAs and Teslascan, both in phosphate-buffered saline and in plasma, also exhibiting low cytotoxicity. The high relaxation rates achieved with these contrast enhancers are promising toward future application in in vivo imaging.

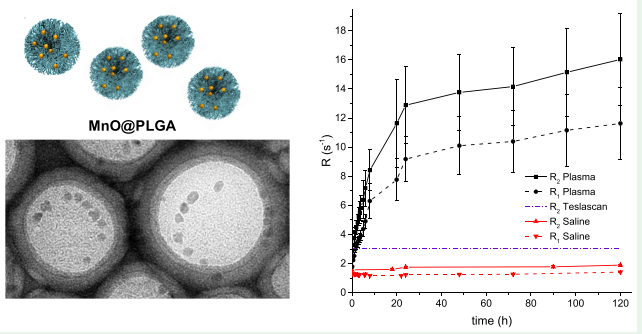

KEYWORDS: *manganese oxide nanoparticles, active polymer coating, magnetic resonance imaging, contrast agents, relaxivity, plasma effect*

INTRODUCTION

Magnetic resonance imaging (MRI) is a noninvasive and efficient medical imaging technique used in daily clinics to visualize the anatomy and physiological processes of patients in real time.[1] Contrast agents (CAs) are often used in MRI, enhancing image spatial resolution and increasing detection sensitivity.[2] The CAs efficiency is measured by their longitudinal (r_1) and transverse (r_2) molar relaxivities, associated with their capability to shorten the spin−lattice (T_1) and spin−spin (T_2) nuclear relaxation times of water protons. The CA relaxivity can be tuned by several methods, resulting in the design of a great diversity of agents.[3] Positive CAs (high r_1) are mainly used for neurological examinations and the diagnosis of neurodegenerative disorders.[4,5] T_1-weighted images are also expected to allow the direct detection of early primary tumors or brain metastasis.[6] In clinics, the most frequently used CAs are gadolinium (Gd)-based probes.[7,8] However, despite their worldwide application, conventional Gd-chelated ion probes exhibit two major limitations: poor sensitivity and, in some cases, long-term accumulation and nephrotoxicity.[9] Although Gd remains the gold-standard CA in clinical MRI, several cases of nephrogenic systemic fibrosis have been reported in patients treated with Gd CAs,[10−14] and as a result, four Gd-based CAs were withdrawn from the market in 2017.[15] Such drawbacks reduced the availability of positive CAs, especially compared with the variety of T_2-based CAs, spawned by the exploitation of superparamagnetic iron oxide nanoparticles (NPs)[16] or fluorinated copolymers.[17] In this context, manganese (Mn) ions and their derivatives have been explored as promising alternatives to positive Gd CAs. Mn^{2+} ions have demonstrated a T_1 contrast power comparable to that of Gd^{III}, increasing the signal intensity of T_1-weighted images.[18] A great advantage of using Mn^{2+} resides in its lower toxicity compared to Gd^{3+} at an

Received: February 20, 2020
Accepted: March 27, 2020
Published: March 27, 2020

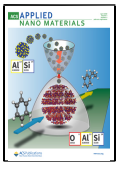

https://dx.doi.org/10.1021/acsanm.0c00474
ACS Appl. Nano Mater. 2020, 3, 3787−3797

equivalent dose.[19] Indeed, Mn is a natural cellular constituent and therefore is often found to act as a protein cofactor.[20,21] Hitherto, examples of Mn^{II} CAs mainly consist of soluble complexes,[22,23] while only a few Mn CAs based on manganese oxide (MnO) nanomaterials,[24−26] metal−organic frameworks,[27] and manganese−oxo clusters have been reported.[28,29] Mangafodipir (trisodium manganese(II) *N*,*N*′-dipyridoxylethylenediamine-*N*,*N*′-diacetate-5,50-bisphosphate) was the first Mn CA initially approved by the Food and Drug Administration and European Medicines Agency to be commercialized as Teslascan for hepatocyte detection.[30] Unfortunately, Teslascan was withdrawn from the market in June 2012 for demonstrated neurotoxicity and commercial reasons;[31,32] thus, there are no presently available Mn CAs. The development of molecular formulations is progressing, in particular through the rational synthesis and evaluation of libraries of variant molecules,[33] but a key step forward in expressing the diagnostic potential of Mn CAs is expected by the contribution of nanotechnology. The ability to rationally manipulate NP features such as size, shape, and surface coating opens up new opportunities in designing diagnostic nanocarriers to selectively target cells, tissues, and metabolic processes.[34,35]

In most studies, MnO particles exhibit very low molar relaxivities, usually in the range 0.2−0.5 mM^{-1} s^{-1}, at least 1 order of magnitude lower than that of free Mn^{2+} ions at the same Mn concentration.[36] Such a small contrast enhancement in MRI has been attributed to the lack of contact between the core Mn atoms and the surrounding water molecules. Recently, 15−20 nm nanoclusters incorporated inside 140 nm and 1.7 μm poly(lactic-*co*-glycolic acid) (PLGA) particles were reported to strongly enhance the MRI contrast under an acidic environment, owing to Mn^{2+} release from the polymer matrix.[37] However, the effectiveness of Mn^{2+} ions is strongly dependent on the interaction with cellular membranes, making the effectiveness of preparations reliant on single Mn ions difficult to validate.[38] On the other side, there is evidence that the interaction of the MnO particle as a whole can be more specifically effective than that of Mn ions: for example, differently shaped particles can display starkly different relaxivities.[39] Also, NPs have the flexibility to be deployed as tunable or activatable systems.[40] Recent work indicates that the relaxivity is extremely sensitive, not only to the particle itself, to the point that it can even be used to distinguish the surface energy of diamagnetic NPs,[41] but also to the coating because it modulates the interactions between water and the NP surface.[42] In the present work, two different kinds of MnO NPs, based on the same cores but with different polymer coatings, were investigated as safe positive CAs with improved MRI performance. One system consists of NPs individually coated with the amphiphilic multidentate polymer poly(isobutylene-*alt*-maleic anhydride), or PMA, which provides individual coverage to each NP. The other system comprises multiple particles embedded in large envelopes made of poly(D,L-lactide-*co*-glycolide) (PLGA NPs).

EXPERIMENTAL SECTION

Materials. Manganese chloride tetrahydrate ($MnCl_2{\cdot}4H_2O$, 99%), sodium oleate (82%), oleic acid (analytical standard), poly(D,L-lactide-*co*-glycolide) (PLGA; MW 24−38 kDa, 50:50), and poly(vinyl alcohol) (PVA; MW 9−10 kDa, 80% hydrolyzed) were purchased from Sigma-Aldrich (St. Louis, MO). Hexane (97%), chloroform, and acetone (99%) were acquired from PanReac AppliChem.

Synthesis of Poly(isobutylene-*alt*-maleic anhydride) (PMA)-Coated Manganese Oxide Nanoparticles (MnO@PMA NPs). The synthesis of oleic acid-coated manganese oxide nanoparticles (MnO NPs) was performed according to a previously reported method.[43] In brief, the metal precursor (manganese oleate) was synthesized via overnight refluxing of a water−ethanol−hexane solution of manganese(II) salt and sodium oleate. Next, thermal decomposition of pure manganese oleate in a high boiling solvent, 1-ocadecene, produced high-quality hydrophobic MnO NPs.[28,43] The so-prepared MnO NPs were subsequently transferred to an aqueous phase by polymeric coating with PMA reacted in an organic solvent with dodecylamine in a 4:3 monomer-to-dodecylamine molar ratio (PMA).[44]

Synthesis of Poly(D,L-lactide-*co*-glycolide) Nanoparticles (PLGA NPs). The carboxyl-group-terminated PLGA NPs (MW 24−38 kDa) were synthesized by a single emulsion solvent evaporation method.[45] Briefly, 12.5 mg of PLGA dissolved in chloroform (1 mL) was added to an aqueous solution of PVA (MW 9−19 kDa, 40 mL, 2% w/w) to form an emulsion under ultrasonic stirring at 40% amplitude for 30 s (twice) in an ice bath (tip-sonicator Branson, Digital Sonifier). The emulsion was left under magnetic stirring to completely evaporate the organic solvent (4 h). The sample was purified by 3-fold centrifugation at 27237 rcf for 15 min at 4 °C (Scanspeed 173OR, Labogene), and the pellet was redispersed twice with a PVA solution (0.3% w/w). Finally, the sample was freeze-dried (Christ, alpha 1−2 LD).

Synthesis of Poly(D,L-lactide-*co*-glycolide)-Coated Manganese Oxide Nanoparticles (MnO@PLGA NPs). The carboxyl group-terminated MnO@PLGA NPs (MW 24−38 kDa) were synthesized through the addition of 8 mg of MnO NPs to an organic solution of PLGA before ultrasonic stirring under the same experimental conditions. Further steps, as mentioned above for the synthesis of PLGA NPs, were followed to entrap multiple MnO NPs inside PLGA NPs.

NP Characterization by Dynamic Light Scattering (DLS) and ζ Potential. The NP size was characterized by DLS using a particle size analyzer (90Plus/BI-MAS, Brookhaven Instruments Corp.) operating at 4 mW of a solid-state laser (λ = 633 nm) with a scattering angle of 173°. Measurements were carried out at 25 °C using a disposable cuvette with 10 mm optical path length. Three measurements per sample were performed to test the repeatability (120 μL, 10 μg mL^{-1} for metal oxide samples, and 25 μg mL^{-1} for polymeric samples). The mean hydrodynamic diameters and standard deviations (SD) were calculated with multimodal analysis using Mie theory, by considering the absolute viscosity and refractive index values of the aqueous medium to be 0.8872 cP and 1.330, respectively. The ζ potential was determined with the same instrument, equipped with a DTS1070 electrode, and data were processed by *ZetaPlus* software. $\zeta-p$ was automatically calculated from the electrophoretic mobility, based on Smoluchowski theory. A viscosity value of 0.8872 cP, a dielectric constant of 78.5, and a Henry function of 1.5 were used for calculations. The mean value from 10 measurements gives one record. Analyses were performed in triplicate for each sample (1 mL, 1 μg mL^{-1} for metal oxide samples, and 3 μg mL^{-1} for polymeric samples).

Morphological Characterization by Transmission Electron Microscopy (TEM). The NP morphology was investigated by TEM (FEI Morgagni at 80 kV), and digital images were obtained by means of a CCD Camera System and the *Leo Image* software. Samples (0.05 μg mL^{-1}) were placed onto a Formvar-coated 300 mesh copper grid (Ted Pella, Inc.). The specimen on the copper grid was negatively stained with uranyl acetate (0.2% w/w) only for polymeric samples. Measure IT Olympus Software was used to determine the particle size distribution by measuring about 150 particles (image processing).

Inductively Coupled Plasma Optical Emission Spectrometry (ICP-OES) Analysis. Mn contents were determined by ICP-OES (ICAP 6300, Thermo Fisher Scientific) and an external calibration methodology, after sample degradation in a mixture of 0.75 mL of HCl (36 vol %) and 0.25 mL of HNO_3 (68% v/v), diluted to 4 mL with Milli-Q water overnight.

https://dx.doi.org/10.1021/acsanm.0c00474
ACS Appl. Nano Mater. 2020, 3, 3787−3797

Scheme 1. Schematic Representation of the Synthesis of (a) MnO@PMA and (b) MnO@PLGA NPs

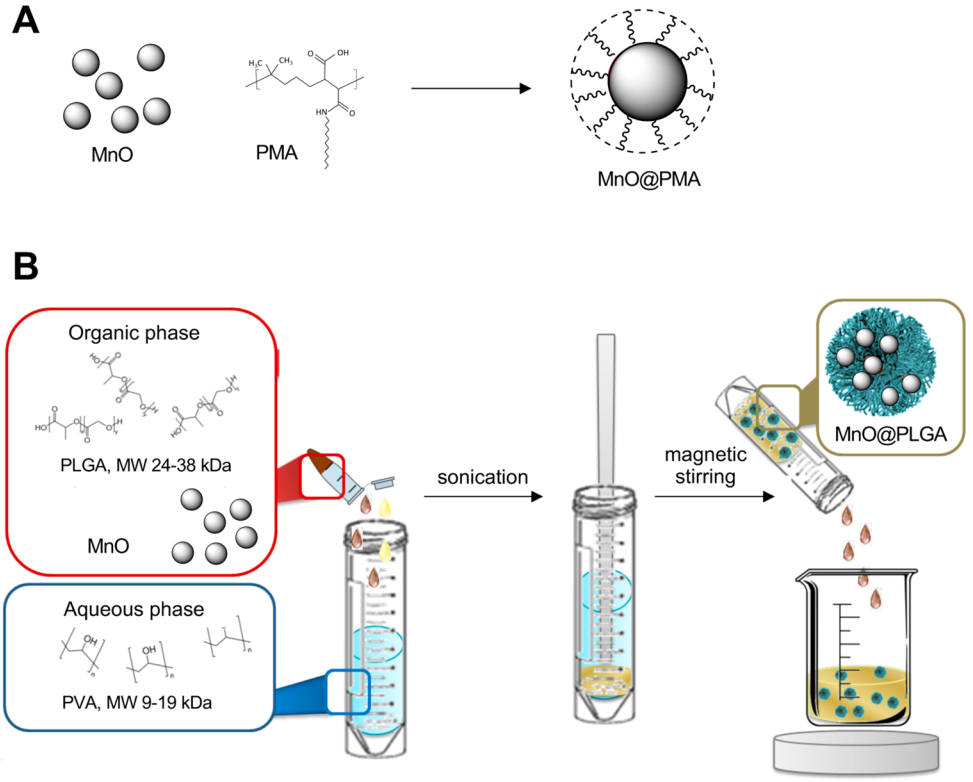

Mn^{2+} Encapsulation Efficiency (%) and Loading ($\mu g\ mg^{-1}$). The encapsulation efficiency expresses the amount of metal oxide NPs loaded inside the PLGA matrix after NP formulation and was calculated as reported in eq 1. Mn^{2+} loading ($\mu g\ mg^{-1}$) is a parameter related to the amount of NPs recovered by ICP analysis after the formulation and theoretical yield (eq 2). ICP analysis was performed by ICP-OES.

$$\text{encapulation efficiency (\%)} = \frac{\text{mass of } Mn^{2+(\mu g)\text{entrapped}}}{\text{mass of } Mn^{2+(\mu g)\text{added}} \text{ reaction}} \times 100 \quad (1)$$

$$\text{loading } (\mu g\ mg^{-1}) = \frac{\text{mass of } Mn^{2+(\mu g)}}{\text{mass of PLGA NPs (mg)}} \quad (2)$$

Relaxometric Analysis. The magnetic properties of MnO@PLGA NPs and other particles were characterized with a 0.5 T (20 MHz) time-domain (TD) NMR benchtop system (Bruker Minispec mq20) with N_2 heating of the sample region. In a typical experiment, 120 μL of NP dispersion was analyzed in 10-mm-diameter NMR glass tubes, filling the bottom to 8 mm depth. Standard CPMG (cp_mb) and saturation recovery (sr_mb) sequences were applied to determine the relaxation times T_2 and T_1, respectively. Measurements were performed at 303 K in different media (saline and plasma mixture). Plasma samples were freshly collected from healthy volunteers. In fact, the NPs cannot be prepared directly in plasma because after preparation they are dispersed in water and cannot be completely lyophilized without altering them. Therefore, stable water dispersions were diluted to the maximum possible concentration with plasma, preparing 58.3% v/v solutions. The relaxation rates R_1 and R_2 were calculated as $1000/T_1$ or T_2, respectively, while the relaxivities r_1 and r_2 coincide with the angular coefficient of the calibration curve R versus concentration, obtained from up to six successive dilutions. CPMG experiments were repeated twice on each sample: once before and once after the longer saturation recovery experiment. This scheme ensures the detection of any rapid change in relaxivity, for example, because of particle precipitation and aggregation.

In Vitro MRI Analysis. The magnetic property of MnO@PLGA NPs was characterized by MRI analysis using a 7 T small-bore magnetic resonance scanner equipped with 450/675 mT/m gradients (slew rate 3400−4500 T/m/s; rise time 140 μs) and a mouse body volume-coil (Bruker, BioSpec 70/30 USR, Paravision 5.1). Samples of 500 μL at different concentrations (from 0.003 to 1.0 mM Mn^{II} ion concentration) were analyzed at 20.6 °C ± 0.1 °C. Rapid Acquisition with Relaxation Enhancement (RARE) with variable repetition time (RAREVTR) and Multi Slice Multi Echo (MSME) sequences were applied to determine T_1 and T_2, respectively. Measurements were performed at 303 K in saline (0.9% NaCl) or in mixtures of saline and plasma (58.3% v/v). The relaxation rates R and relaxivities r were calculated as described above. The software processes the T_1 map and provides the MRI images, in which the dynamic contrast is shown as a bright signal.

Cell Culture. The HeLa cervical cancer cell line was used as the in vitro cell culture model. Cells were cultured in high glucose Dulbecco's modified Eagle medium, supplemented with 10% heat-inactivated fetal bovine serum, 2 mM L-glutamine, 100 U mL^{-1} penicillin, and 0.1 mg mL^{-1} streptomycin at 37 °C in a humidified atmosphere containing 5% CO_2. At confluence, the cells were treated using trypsin−ethylenediaminetetraacetic acid in a 1:4 to 1:6 split ratio or used for experiments. All cell culture materials were supplied by Euroclone S.p.A. (Milano, IT).

MTT Assay. The in vitro cytotoxicity of MnO@PMA, MnO@PLGA, and PLGA NPs was tested on HeLa cells through an MTT assay (CellTiter 96 Non-Radioactive Cell Proliferation Assay, Promega). Cells were seeded in a 96-well plate at a density of 5×10^3 cells $well^{-1}$ and incubated for 24 h. Then, the cells were incubated with different amounts of the NPs to be tested, with six replicates for each concentration. According to the manufacturer's instructions, at the end of the exposure time (24, 48, and 72 h), MTT was added and a formazan product was detected after 4 h at 37 °C, reading the absorbance at 570 nm with an EnSight Multimode Plate Reader (PerkinElmer) and subtracting the absorbance of background at 620 nm. The results were obtained by normalizing the untreated cells set at 100% and expressed as percentage ± SD.

https://dx.doi.org/10.1021/acsanm.0c00474
ACS Appl. Nano Mater. 2020, 3, 3787−3797

X-ray Diffraction (XRD). For XRD characterization, a D8 Advance powder diffractometer (Bruker) was used with Cu $K\alpha_1$ radiation (λ = 1.5418 Å) and a secondary-beam monochromator. The powder was added to a quartz sample holder and measured.

RESULTS AND DISCUSSION

Synthesis and Chemical−Physical Characterization of MnO@PLGA and MnO@PMA NPs. A schematic representation of the preparation of MnO@PLGA and MnO@PMA NPs is illustrated in Scheme 1. In a first setting, a biodegradable PLGA polymer matrix was used to trap and carry MnO NPs, presynthesized in an organic solvent as MnO nanocrystals stabilized by oleic acid coating, obtaining MnO@PLGA NPs (Scheme 1B). This strategy was aimed at concentrating a large number of MnO NPs inside a nanocarrier that could allow the simultaneous delivery of a sufficient amount of Mn, to cause a localized increase in the T_1 relaxivity, while decreasing the metal toxicity associated with free ionic Mn^{2+}. The aim of this study was to compare the magnetic properties as T_1 CAs and the biological effects of MnO@PLGA NPs with those of colloidally stable MnO NPs that were obtained by individually wrapping the same paramagnetic MnO nanocrystals into an amphiphilic multidentate polymer PMA endowed with a high affinity for hydrophobic particles (Scheme 1A).

As-synthesized, surfactant-coated MnO nanocrystals[28,43] showed a hydrodynamic diameter of 15.9 ± 0.2 nm in chloroform, as measured by DLS (Figure 1A), in agreement with TEM (Figure 1B), which exhibited homogeneous quasi-spherical NPs of 9.7 ± 1.3 nm. Water-soluble MnO (MnO@PMA) NPs with high colloidal stability were obtained by coating MnO nanocrystals with PMA, synthesized by condensing PMA with dodecylamine, as previously reported.[44] MnO@PMA NPs exhibited a hydrodynamic diameter of 17.7 ± 0.8 nm (Figure S1E) and a diffractogram typical of MnO nanocrystals covered with a relatively thick layer of amorphous polymer (Figure S2).[46] PLGA NPs were prepared by a single emulsion method (see the Methods section).[45] To obtain MnO@PLGA NPs, MnO nanocrystals were added to a PLGA (MW 24−38 kDa) solution in chloroform, mixed with an aqueous solution of 2% PVA (MW 9−19 kDa), sonicated, and freeze-dried. Both empty PLGA NPs and MnO@PLGA NPs were colloidally stable in aqueous media and showed comparable sizes [150.5 ± 8.0 and 163.0 ± 3.3 nm, respectively; Figure 1A], with negative surface charge (ζ potential of −33.5 ± 0.35 and −32.1 ± 0.99 mV, respectively). Data from TEM were consistent with the DLS size and showed that the NPs maintained their spherical shape after MnO loading (Figures 1C,D and S1). Figure 1D clearly shows that several MnO nanocrystals were included in each PLGA polymer NP. Notably, the nanocrystals were preferentially located inside the inner core, rather than at the outer shell. Both DLS and TEM size distributions suggest a high degree of monodispersity (Table 1 and Figures 1 and S1). We thus concluded that the encapsulation of metal oxide NPs did not significantly affect the overall shape, dimension, and charge of PLGA NPs.

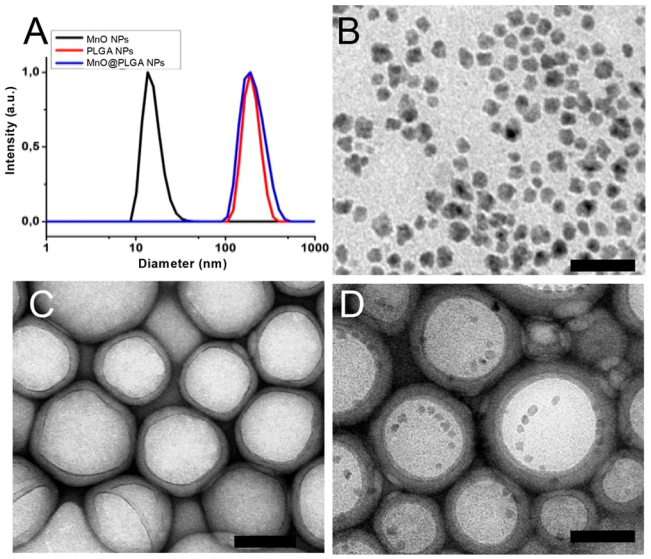

Figure 1. (A) Hydrodynamic diameters of MnO, PLGA, and MnO@PLGA NPs measured by DLS. TEM images of (B) MnO (scale bar = 50 nm), (C) PLGA, and (D) MnO@PLGA NPs (scale bar = 100 nm). Samples were negatively stained with uranyl acetate (0.2% w/w).

Table 1. DLS and ζ-Potential Data of MnO NPs, PLGA NPs, and MnO@PLGA NPs

	TEM diameter (nm)	DLS diameter (nm)	PDI	ζ (mV)
MnO NPs	9.7 ± 1.3	15.9 ± 0.2	0.130 ± 0.034	
MnO@PMA	9.7 ± 1.3[a]	17.7 ± 0.8	0.296 ± 0.22	−40.8 ± 0.70
PLGA NPs	129.5 ± 35.1	150.5 ± 8.0	0.058 ± 0.028	−33.5 ± 0.3
MnO@PLGA NPs	132.8 ± 41.9	163.0 ± 3.3	0.117 ± 0.013	−32.1 ± 0.99

[a]Same as those of MnO NPs; PMA is not visible at TEM.

We assessed the colloidal stability of MnO@PMA and MnO@PLGA NPs in physiological phosphate-buffered saline (PBS; pH 7.2) to estimate their potential for biomedical applications. MnO@PMA NPs were highly stable in water and PBS for at least 10 days (Figure 2A), after an initial swelling from the size values indicated in Table 1 to slightly higher ones, closer to 200 nm. This difference between the first measurable value and the equilibrium value is in line with the smaller diameters measured by TEM, which were performed in vacuum and therefore do not reflect any swelling. MnO@PLGA NPs were first lyophilized for storage, showing a stability of at least 10 days after reconstitution in PBS, according to DLS data (Figure 2B). An Mn^{2+} loading of 13.8 ± 2.2 μg mg^{-1} of PLGA, corresponding to an encapsulation efficiency (EE%) of 9.65 ± 1.31%, was determined by ICP-OES analysis and proved to be reproducible from batch to batch. For MnO@PMA, a Mn^{2+} loading of 36 μg mg^{-1} of PMA was obtained.

Relaxometric Determination of the Contrast Power of MnO@PLGA and MnO@PMA NPs in an Aqueous Buffer and Human Plasma. Relaxivity (r) measurements for MnO@PMA and MnO@PLGA NPs were conducted at 310 K to evaluate the ability of Mn-bearing NPs to reduce the relaxation rates (R) of water protons at 0.5 T, at a temperature close to those of real biosystems. The longitudinal (T_1) and transverse (T_2) relaxation times of MnO@PMA and MnO@PLGA NPs were first measured in PBS with the typical sequences (CPMG and saturation recovery) used for the characterization of magnetic NPs.[47] MnO@PMA NP

https://dx.doi.org/10.1021/acsanm.0c00474
ACS Appl. Nano Mater. 2020, 3, 3787−3797

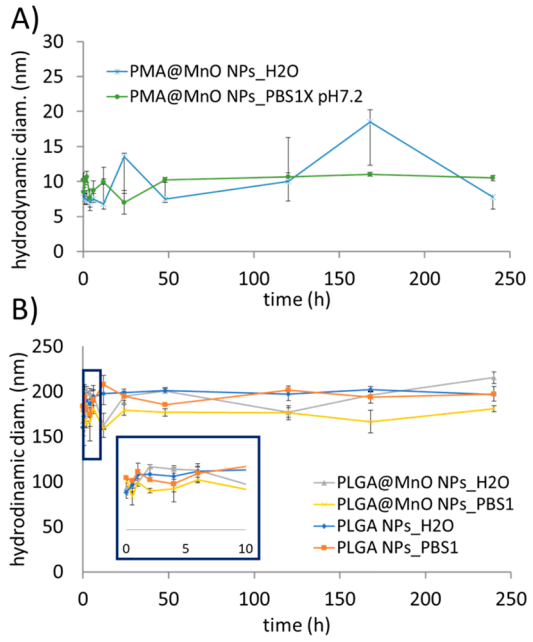

Figure 2. Colloidal stability of (A) MnO@PMA NPs and (B) PLGA NPs and lyophilized MnO@PLGA NPs in water and PBS over 10 days, measured by DLS analysis. The inset shows the evolution during the initial 10 h.

relaxation rates (R_1 and R_2, calculated as $1/T_1$ and $1/T_2$, respectively, plotted in Figure 3A) were found to linearly depend on the CA concentration, within a wide range (up to the maximum obtainable Mn^{2+} concentration of around 0.5 mM), thereby confirming NP stability and the absence of aggregation. The longitudinal and transverse relaxivities (r_1 and r_2, determined as the slope in the R vs $[Mn^{2+}]$ plot; Figure 3) in water were estimated to be 7.7 and 10.5 mM^{-1} s^{-1}, respectively (Figure 3A). The r_2/r_1 ratio is an important parameter to estimate whether a contrast enhancer can serve as either T_1 or T_2 CA. T_1 CAs, such as paramagnetic chelates, usually exhibit r_2/r_1 ratios in a range of 1−2.[48] MnO@PMA NPs are thus well suited as T_1 CAs, having r_2/r_1 = 1.2 and high r_1 absolute relaxivity values, in line with reportedly excellent NPs.[49] In addition, MnO@PMA NPs maintained constant relaxivity values in water for at least 24 h (Figure S3). Figure 3B indicates that the linearity of the relaxation rate with the concentration was maintained for MnO@PLGA in PBS, up to a concentration of 11 mM. The encapsulation of MnO nanocrystals into PLGA as MnO@PLGA NPs increased the solubility, and thus the maximum obtainable concentration of Mn^{2+} in the dispersion increases to 11 mM.

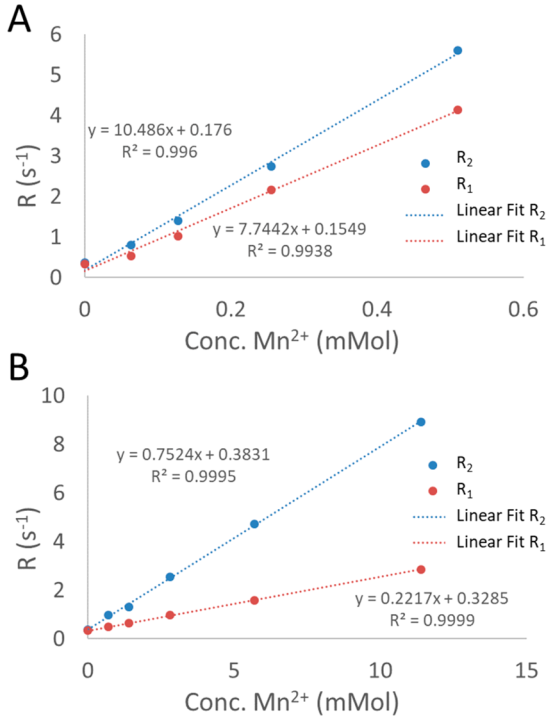

Figure 3. Relaxivities r_1 and r_2 calculated by measuring the relaxation rate at different dilutions of (A) MnO@PMA in PBS (R_2, $y = 10.5x + 0.2$, $R^2 = 0.996$; R_1, $y = 7.74x + 0.2$, $R^2 = 0.994$) and (B) MnO@PLGA NPs in PBS (R_2, $y = 0.75x + 0.4$, $R^2 = 0.9995$; R_1, $y = 0.22x + 0.3$, $R^2 = 0.9999$).

Interestingly, the absolute values of the relaxation rates are not much higher than those achievable by PMA-coated NPs at lower concentrations, resulting in much smaller values of r_1 and r_2 (r_1 = 0.22 mM^{-1} s^{-1}; r_2 = 0.75 mM^{-1} s^{-1}; r_2/r_1 = 3.4; Figure 3C). This variation of more than 1 order of magnitude is due to the presence of the PLGA matrix in MnO@PLGA NPs, which is likely to reduce the CA interaction with water molecules, thereby decreasing the spin−spin and spin−lattice relaxation from the CA to the surrounding medium much more pronouncedly, compared to the thin PMA layer in MnO@PMA NPs.[50] The detected 3-fold increase of the r_2/r_1 ratio, in comparison to MnO@PMA NPs, also points toward a difference in accessibility because T_2 relaxation is related to longer-range effects compared to T_1, and the ratio changes because r_1 was more strongly affected by PLGA encapsulation. Importantly, also the MnO@PLGA NP relaxivities remained constant over 24 h in water (Figure S3). To evaluate the contrast power of the NPs, their longitudinal relaxivity was then compared with the Teslascan data available in the literature (r_1 = 1.85 mM^{-1} s^{-1}; r_2 = 2.18 mM^{-1} s^{-1}; r_2/r_1 = 1.2).[51] The relaxation of MnO@PMA was found to be even higher than that reported for Teslascan, suggesting a superior efficacy for MnO@PMA NPs as a contrast enhancer in vitro, compared to commercial CAs. Note that this is an improvement also over many Mn systems presented in the literature, which mostly present lower absolute r_1 values[26] or very high r_2/r_1 ratios.[27] In contrast, the relaxation of MnO@PLGA NPs was 2.7 times lower than that of Teslascan. However, in order to fully appreciate the potential of these composite NPs for future in vivo MRI applications, the relaxation times for both MnO@PMA and MnO@PLGA NPs were further analyzed in human plasma (Figures 4 and 5). For the experiments in Figure 4, we prepared solutions with different amounts of MnO particles, selected to start with roughly the same absolute R_1.

In plasma, the MnO@PMA r_1 and r_2 values increased immediately after dispersion to 14.5 and 16 mM^{-1} s^{-1}, respectively, whereas the r_2/r_1 ratio remained near 1.1. For MnO@PLGA, the relaxivities measured immediately after sample preparation were 0.68 m^{-1} s^{-1} (r_1) and 0.71 mM^{-1} s^{-1} (r_2) (Figure 3SB,C). This also brought the ratio close to 1, indicating a different mechanism of interaction, which is to be expected because the interaction between the NPs embedded in the PLGA coating and water is mediated by PLGA itself, which is sensitive to the presence of various plasma molecules.

https://dx.doi.org/10.1021/acsanm.0c00474
ACS Appl. Nano Mater. 2020, 3, 3787−3797

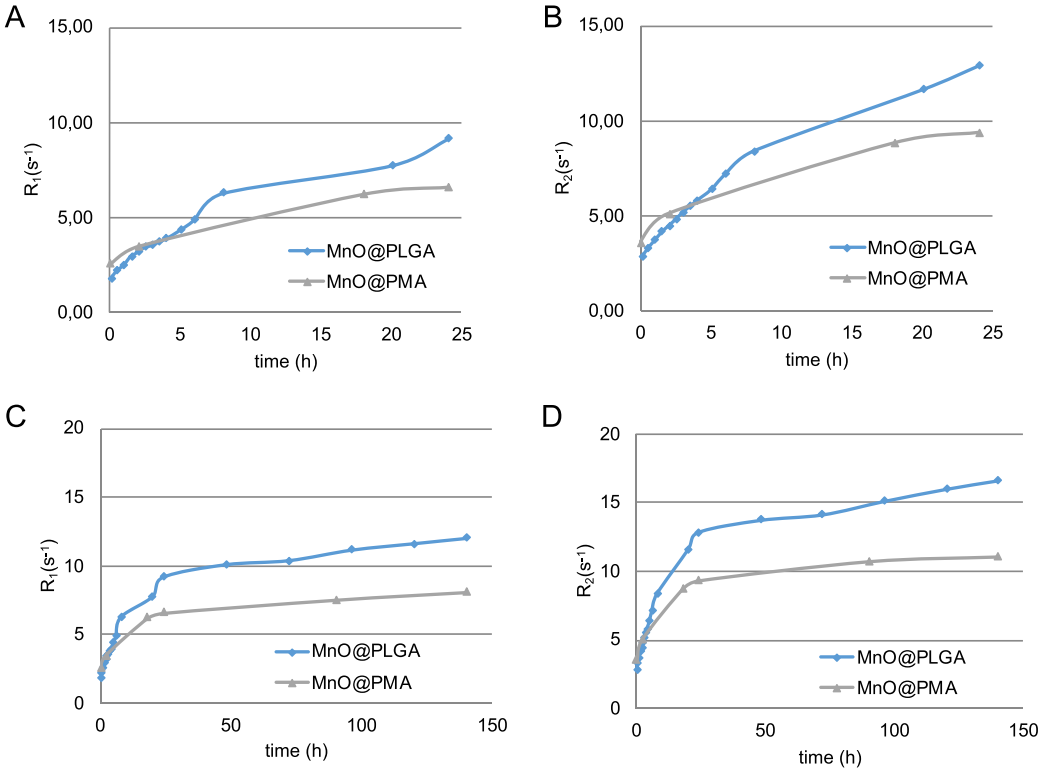

Figure 4. Relaxation rates R_1 and R_2 of MnO@PLGA and MnO@PMA NPs (120 μL, 917 μg mL^{-1} MnO@PLGA NPs, and 88 μg mL^{-1} MnO@PMA) in plasma from three different donors for 24 h (A and B, respectively) and for 6 days (C and D, respectively).

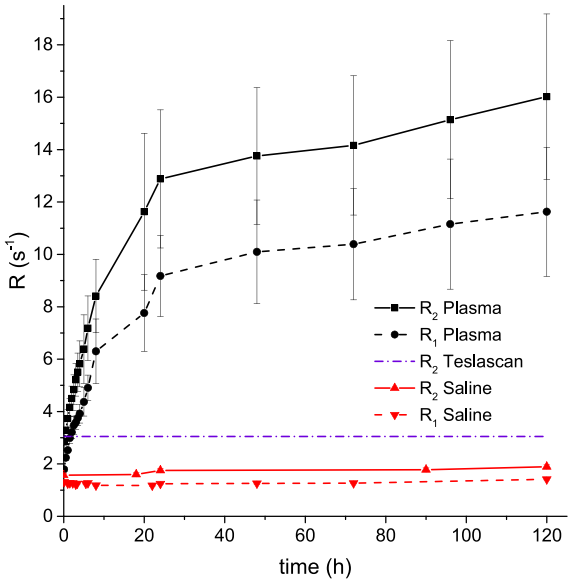

Figure 5. R_1 and R_2 values for MnO@PLGA in PBS and plasma, up to 120 h. Both samples contained 100 mg mL^{-1} CA, corresponding to 1.4 mmol of Mn^{2+}. The dashed line represents the expected R_2 relaxivity for the same amount of Teslascan. The values presented for plasma are an average from three experiments performed with plasma from different donors. The SDs for measurements conducted in PBS were <1%.

Still, the absolute values were low, as observed in the assessment of the Gd response in plasma, where Gd forms complexes with blood proteins that partially mask the paramagnetic effect.[19]

Both MnO@PMA and MnO@PLGA NPs showed kinetic profiles in plasma that were significantly different from those measured in PBS (Figure 4). In plasma, we observed a burst increase in both R_1 and R_2 within the first 6 h, followed by a change in the slope, leading to a milder increase during the subsequent 24 h. This experiment was extended for 120 h, confirming the trend.

Because the effect appeared to be much more pronounced in MnO@PLGA, with an increase of 1 order of magnitude, we replotted the data from plasma and PBS in Figure 5, also reporting r_2. The wide error bars present in the figure indicate a high sensitivity to the specific composition of the plasma from different donors. Still, the kinetic profile was consistently the same, with both relaxation values surpassing those of Teslascan over time. This confirms that the increased relaxation properties are inherent to the evolution of the material and independent of the inhomogeneities of the environment composition. An estimate of r_1 and r_2, based on the ratio between the maximum R values and concentration, yielded 11.38 mM^{-1} s^{-1} for r_2 and 8.26 mM^{-1} s^{-1} for r_1. We assumed that the increase of R_1 and R_2 over time was due to a release of either Mn^{2+} ions or MnO NPs from the carriers, resulting in a more effective interaction with the surrounding medium. The values estimated above also produced an r_2/r_1 ratio of 1.38, indicating that the most relevant mechanism is the interaction of NPs with water.

The phenomena discussed above are summarized in Table 2, where both the high intrinsic efficiency of MnO@PMA NPs and the peculiar behavior of MnO@PLGA in plasma clearly stand out.

Possible mechanisms for the latter effect include swelling of the polymeric matrix or faster degradation of the PLGA polymer in plasma compared to PBS. Indeed, released MnO

https://dx.doi.org/10.1021/acsanm.0c00474
ACS Appl. Nano Mater. 2020, 3, 3787−3797

Table 2. Summary of the r_1 and r_2 Values of the Novel NPs and Teslascan Benchmark[a]

sample	r_1	r_2	r_2/r_1	time evolution r_1
		In PBS		
MnO@PMA	7.7	10.4	1.35	stable
MnO@PLGA	0.24	0.82	3.4	stable
Teslascan	1.85	2.18	1.2	stable
		In Plasma		
MnO@PMA	*14.5*	*16.0*	1.1	increase to 31 ± 1
MnO@PLGA	*0.68*	*0.71*	1.05	increase to *8.3* ± *1.5*

[a]The relaxivities are expressed in mM^{-1} s^{-1}. The values in italics are not rigorously obtained as a slope but rather estimated using a single point at a known concentration. The SDs omitted for clarity are less than 4% except for MnO@PLGA, where the differences between plasma donors increase the variability.

NPs were expected to produce also a progressive and sustained release of Mn^{2+} ions, with a concomitant increase in the T_1-weighted MRI signal. It is likely that the small aqueous CAs exhibited higher relaxation rates by reducing molecular motion due to interactions with serum proteins.[52,53] In support of this interpretation, we observed that Mn^{2+} ions in plasma led to greater T_1 shortening compared to PBS, in a wide concentration range (Table 3). On the other hand, ions

Table 3. R_1 and R_2 Values of $MnCl_2$ Solutions in PBS (pH 7.4, 100 mM) and Plasma (4 h of Incubation) Measured at 37 °C and in a TD NMR Spectrometer Working at the Clinical MRI Field (1.5 T)[a]

$[Mn^{2+}]$ (mM)	R_1 in PBS (ms)	R_1 in plasma (ms)	R_2 in PBS (ms)	R_2 in plasma (ms)
0.25	1.5	10.4	19.7	23.1
1	5.5	20.7	66.3	56.9
10	50.9	105.2	609.8	530.2
r ($mmol^{-1}$ s^{-1})	5.06	9.58	60.47	52.26

[a]Errors were always below 1%. From the values, r was also calculated and is reported in the table.

produced by the dissolution of $MnCl_2$ also produced a very high r_2/r_1 ratio, around 10 in PBS and 5 in plasma, supporting the hypothesis of the relaxation being due to the whole NPs. In itself, T_1 reduction can be attributed also to ions,[38] but a low r_2/r_1 ratio is typical of whole NPs. Compared to the literature,[37] it is important to note that we used PLGA with low molecular weight: it is commonplace for the MW of a polymer coating to regulate its mobility and entanglement and thus access to its surface.[54]

Phantom Analysis of Contrast Enhancement Using MnO@PLGA NPs by MRI. The longitudinal relaxation times of polymeric NPs were measured by an MRI scanner at 7 T to preliminarily investigate the MRI positive contrast power. The T_1-weighted images showed a clear dose-dependent signal in both PBS and plasma (Figure 6A,B), in agreement with the TD NMR data. The r_1 values of the NPs remained constant in PBS, while it increased over time in plasma. MRI analysis thus confirmed the TD NMR data. No contrast was detected in both physiological media and plasma for the control PLGA NPs (data not shown).

Relaxation rates as a function of the Mn^{2+} ion concentration (Figures 6C,D and S4) clearly demonstrated that the values of r_1 remained stable in PBS for at least 6 h (0.201 ± 0.008 mM^{-1} s^{-1}). As expected from TD NMR and MRI studies, the relaxivity of MnO@PLGA NPs increased over time at all tested concentrations, in the presence of plasma (r_1 raised from 0.217 to 0.532 mM^{-1} s^{-1}). In particular, it was observed that the initial r_1 value in plasma matched the r_1 values in PBS. This observation confirmed that no sample degradation occurred within minutes after MnO@PLGA NP dispersion in plasma. To check whether the effect of all NPs or Mn^{2+} ions was prevalent in either PBS or plasma, we measured the release of Mn^{2+} ions in both media. As indicated in Figure S5, the particles were partly dissolved, but only after several hours and never completely. These data support the opsonization hypothesis, according to which the time-dependent r_1 enhancement was caused by the release of MnO CA from PLGA NPs in plasma, most likely due to matrix swelling rather than to polymer degradation. From the MRI data of MnO@PLGA NPs, 0.026 mM Mn^{2+} was the minimum concentration that could provide a detectable signal.

Investigation of the Cytotoxicity Profile for MnO@PLGA and MnO@PMA NPs. The toxicity of Mn-based CAs is primarily due to the action of Mn^{2+} as a calcium channel blocker with effects on muscle electrophysiology and contractility. This effect has limited the use of Mn^{2+} salts as paramagnetic CAs for in vivo diagnosis.[55,56] In addition, Mn^{2+} complexes are relatively unstable in vivo and tend to dissociate in biological media. Indeed, Mn ions can be displaced by other divalent cations, such as Ca^{2+}, Mg^{2+}, or Zn^{2+}. Hence, some concerns exist about the potential long-term toxicity associated with the use of Mn CAs.[57−59] Therefore, to assess the potential of MnO@PMA and MnO@PLGA NPs as CAs, we investigated their toxicity in vitro. Cytotoxicity tests using representative HeLa cancer cells demonstrated that both PLGA NPs and MnO@PLGA NPs were safe in the tested concentration range (Figure 7). The low toxicity of the NPs was confirmed by reactive oxygen species (ROS) assay (Figure S6): the amount of ROS, detected after 24 h, did not induce any toxic effect, as demonstrated by MTT analysis. Table 4 correlates the PLGA weight and Mn^{2+} concentration. After 72 h of incubation, the viability of the treated cells was comparable to that of the control. In contrast, MnO@PMA exhibited mild time- and dose-dependent cytotoxicity above 15 nM (Figure 7), suggesting that the cytotoxicity observed using MnO@PMA NPs was prevented by the PLGA coating.

CONCLUSIONS

In summary, two Mn-based nanoprobes were investigated as safer and effective positive contrast enhancers, with the objective of providing alternatives to Gd and Teslascan. MnO@PMA NPs showed higher longitudinal relaxivity compared to Gd-based CAs and Teslascan,[60] while maintaining a low r_2/r_1 ratio, in both PBS and plasma, also exhibiting low cytotoxicity. An improved biodegradable Mn-based nanocomposite, consisting of MnO nanoclusters incorporated into PLGA NPs (MnO@PLGA), was synthesized. MnO@PLGA NPs offered the advantage of lower toxicity with 3-fold higher T_1 contrast power compared to Gd and Teslascan. Our water-soluble MnO@PLGA CAs exhibited a very pronounced dose- and time-dependent r_1 increase in plasma, possibly because of the use of relatively short PLGA compared to the literature, thereby favoring the release of active NPs in plasma while maintaining a high particle stability in PBS. A comparison with the relaxation phenomena induced by Mn ions in the same solutions, which are characterized by ratios

https://dx.doi.org/10.1021/acsanm.0c00474
ACS Appl. Nano Mater. 2020, 3, 3787−3797

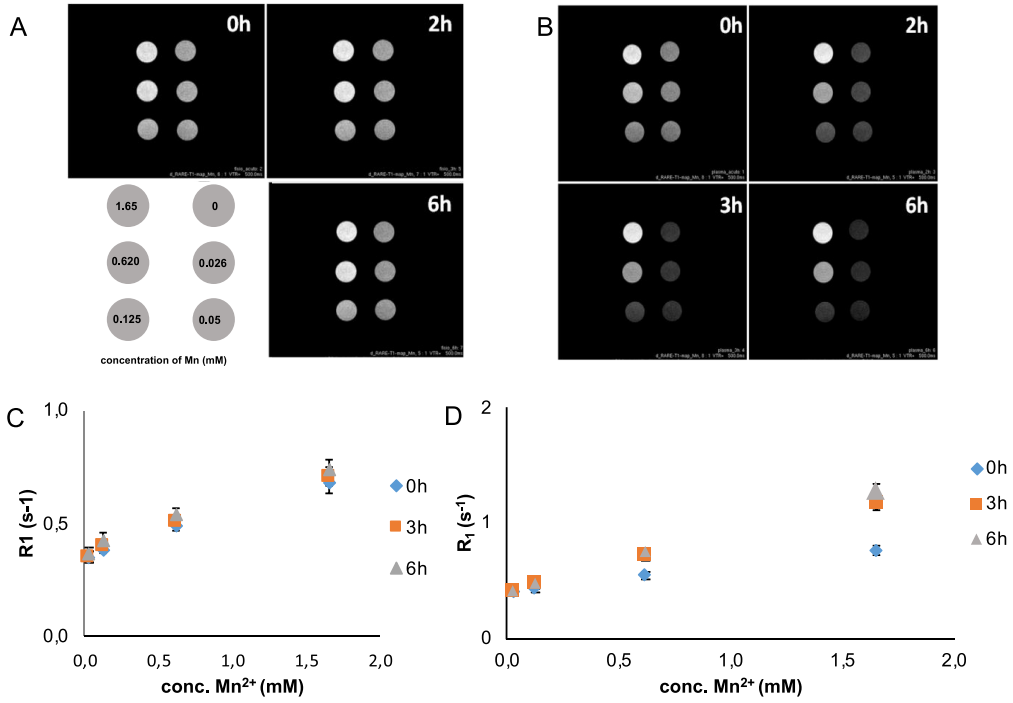

Figure 6. T_1-weighted images of MnO@PLGA NPs at different concentrations of Mn^{2+} ions (in the range 0−1.65 mM) in (A) PBS and (B) plasma. R_1 of MnO@PLGA NPs in (C) PBS and (D) plasma as a function of the Mn^{2+} concentration (0−1.65 mM) and time (0−6 h).

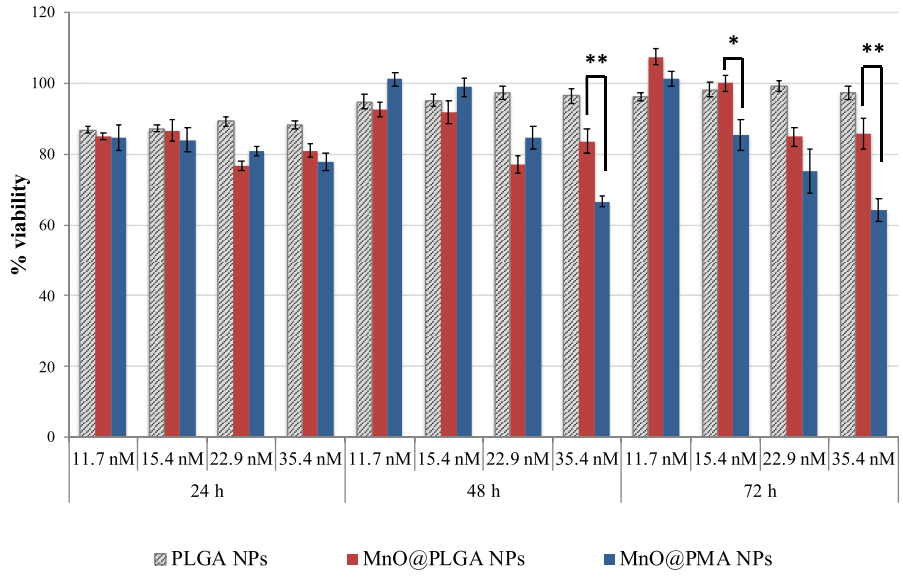

Figure 7. In vitro cytotoxicity study in HeLa cells. The cell viability was assessed by MTT assay. Cells treated for 72 h with PLGA NPs, MnO@PLGA NPs, and MnO@PMA NPs. Reported values are the mean of five replicates ± s.e. normalized on the proliferation of untreated cells. *, $P < 0.05$; **, $P < 0.01$ (Student's t test).

Table 4. Mn Ion Concentration Relative to the NP Dosages Used in Bioavailability Experiments

$[Mn^{II}]$ (nM)	$[Mn^{II}]$ ($\mu g\ mL^{-1}$)	[MnO@PLGA NPs] ($\mu g\ mL^{-1}$)	[MnO@PMA NPs] ($\mu g\ mL^{-1}$)
11.7	0.6	43.5	16.7
15.4	0.8	58.0	22.2
22.9	1.3	94.2	36.1
35.4	1.9	137.7	52.8

close to 10 and thus are very far from the ideal value of 1, indicates that the measured properties are the unique result of the release of entire NPs. This unforeseen property is particularly attractive in view of clinical translation: the localized release of CAs at target cells or tissues by either passive (i.e., via the enhanced permeability and retention effect) or active (i.e., exploiting NP functionalization with selective ligands) targeting offers the chance to strongly improve the signal intensity over time, further enhancing the MRI sensitivity. The use of these CAs brings new challenges for clinical application. Commercially available CAs are nonspecific, whereas PLGA and PMA polymers have been proposed as basic envelopes, suitable for subsequent surface

https://dx.doi.org/10.1021/acsanm.0c00474
ACS Appl. Nano Mater. 2020, 3, 3787−3797

bioengineering with selective ligands (e.g., small molecules, peptides, and antibodies) for molecular recognition associated with specific disorders. In addition, therapeutic agents or secondary imaging components can be loaded into PLGA NPs, resulting in multifunctional theranostics for early detection, diagnosis, and personalized treatments. The combination of all of these properties makes MnO@PMA and MnO@PLGA NPs promising nanoprobes for molecular imaging.

■ ASSOCIATED CONTENT

Supporting Information

The Supporting Information is available free of charge at https://pubs.acs.org/doi/10.1021/acsanm.0c00474.

TEM images, DLS size distribution of NPs (Figure S1), XRD diffractogram of MnO@PMA NPs (Figure S2), R_1 and R_2 stabilities of NPs (Figure S3), release profile of Mn^{2+} (Figure S4), T_1-weighted images of different concentrations of MnO@PLGA NPs (Figure S5), and percentage of ROS accumulation in the HeLa cell line (Figure S6) (PDF)

■ AUTHOR INFORMATION

Corresponding Author

Miriam Colombo − *NanoBioLab, Department of Biotechnology and Biosciences, University of Milano-Bicocca, 20126 Milan, Italy;* orcid.org/0000-0003-3428-5668; Phone: +39 02 6448 3388; Email: miriam.colombo@unimib.it

Authors

Michele Mauri − *Department of Material Science, University of Milano-Bicocca, 20125 Milan, Italy;* orcid.org/0000-0002-7777-9820

Veronica Collico − *NanoBioLab, Department of Biotechnology and Biosciences, University of Milano-Bicocca, 20126 Milan, Italy*

Lucia Morelli − *NanoBioLab, Department of Biotechnology and Biosciences, University of Milano-Bicocca, 20126 Milan, Italy*

Pradip Das − *NanoBioLab, Department of Biotechnology and Biosciences, University of Milano-Bicocca, 20126 Milan, Italy;* orcid.org/0000-0001-8898-331X

Isabel García − *CIC biomaGUNE, Basque Research and Technology Alliance, 20014 Donostia−San Sebastián, Spain; Centro de Investigación Biomédica en Red, Biomateriales, Bioingeniería y Nanomedicina, 20014 Donostia−San Sebastián, Spain*

Jesus Penaranda Avila − *NanoBioLab, Department of Biotechnology and Biosciences, University of Milano-Bicocca, 20126 Milan, Italy*

Michela Bellini − *NanoBioLab, Department of Biotechnology and Biosciences, University of Milano-Bicocca, 20126 Milan, Italy*

Rany Rotem − *NanoBioLab, Department of Biotechnology and Biosciences, University of Milano-Bicocca, 20126 Milan, Italy*

Marta Truffi − *Nanomedicina Laboratory, Department of Biomedical and Clinical Sciences "L. Sacco", 20157 Milan, Italy*

Fabio Corsi − *Nanomedicina Laboratory, Department of Biomedical and Clinical Sciences "L. Sacco", 20157 Milan, Italy; Breast Unit, Surgery Department, ICS Maugeri IRCCS, 27100 Pavia, Italy*

Roberto Simonutti − *Department of Material Science, University of Milano-Bicocca, 20125 Milan, Italy;* orcid.org/0000-0001-8093-517X

Luis M. Liz-Marzán − *CIC biomaGUNE, Basque Research and Technology Alliance, 20014 Donostia−San Sebastián, Spain; Centro de Investigación Biomédica en Red, Biomateriales, Bioingeniería y Nanomedicina, 20014 Donostia−San Sebastián, Spain; Ikerbasque, Basque Foundation for Science, 48013 Bilbao, Spain;* orcid.org/0000-0002-6647-1353

Davide Prosperi − *NanoBioLab, Department of Biotechnology and Biosciences, University of Milano-Bicocca, 20126 Milan, Italy; Breast Unit, Surgery Department, ICS Maugeri IRCCS, 27100 Pavia, Italy;* orcid.org/0000-0003-4577-9575

Complete contact information is available at: https://pubs.acs.org/10.1021/acsanm.0c00474

Author Contributions

†These authors contributed equally to this work. The manuscript was written through contributions of all authors. All authors have given approval to the final version of the manuscript.

Funding

Financial support from the Italian Ministry of University and Research (MIUR) through grant "Dipartimenti di Eccellenza-2017" to the University of Milano-Bicocca, Department of Biotechnology and Biosciences, and Spanish Ministerio de Ciencia e Innovación (Grant MAT2017-86659-R) is acknowledged.

Notes

The authors declare no competing financial interest.

■ ACKNOWLEDGMENTS

We thank T. Canu and A. Esposito (IRCCS San Raffaele Hospital, Milano) for magnetic resonance service. We thank Silvia Ferrario (Graftonica) for performing XRD.

■ ABBREVIATIONS

CA = contrast agent
DLS = dynamic light scattering
ICP-OES = inductively coupled plasma optical emission spectrometry
MRI = magnetic resonance imaging
NP = nanoparticle
PBS = phosphate-buffered saline
PDI = polydispersity index
PLGA = poly(lactic-*co*-glycolic acid)
PMA = poly[isobutene-*alt*-maleic anhydride]-*graft*-dodecylamine (75%) polymer
r_1 = longitudinal relaxivity
r_2 = transverse relaxivity
R_1 = longitudinal relaxation rate
R_2 = transverse relaxation rate
T_1 = spin−lattice relaxation time
T_2 = spin−spin relaxation time
TD NMR = time-domain nuclear magnetic resonance
TEM = transmission electron microscopy
ξ = zeta potential

■ REFERENCES

(1) Cleary, K.; Peters, T. M. Image-guided interventions: technology review and clinical applications. *Annu. Rev. Biomed. Eng.* **2010**, *12*, 119−142.

(2) Strijkers, G. J.; Mulder, W. J. M.; van Tilborg, G. A. F.; Nicolay, K. MRI contrast agents: current status and future perspectives. *Anti-Cancer Agents Med. Chem.* **2007**, *7*, 291−305.

(3) De León-Rodríguez, L. M.; Martins, A. F.; Pinho, M. C.; Rofsky, N. M.; Sherry, A. D. Basic mr relaxation mechanisms and contrast agent design. *J. Magn. Reson. Imaging* **2015**, *42*, 545−565.
(4) Babeu, J. P.; Boudreau, F. Hepatocyte nuclear factor 4-alpha involvement in liver and intestinal inflammatory networks. *World J. Gastroenterol.* **2014**, *20*, 22−30.
(5) Yousry, T. A.; Major, E. O.; Ryschkewitsch, C.; Fahle, G.; Fischer, S.; Hou, J.; Curfman, B.; Miszkiel, K.; Mueller-Lenke, N.; Sanchez, E.; Barkhof, F.; Radue, E. W.; Jäger, H. R.; Clifford, D. B. Evaluation of patients treated with natalizumab for progressive multifocal leukoencephalopathy. *N. Engl. J. Med.* **2006**, *354*, 924−933.
(6) Ross, M. R.; Schomer, D. F.; Chappell, P.; Enzmann, D. R. MR imaging of head and neck tumors: comparison of T_1-weighted contrast-enhanced fat-suppressed images with conventional T_2-weighted and fast spin-echo T_2-weighted images. *AJR, Am. J. Roentgenol.* **1994**, *163*, 173−178.
(7) Niendorf, H. P.; Felix, R.; Laniado, M.; Schörner, W.; Kornmesser, W.; Claussen, C. Magnetic resonance imaging of intracranial tumors using gadolinium-DTPA. Initial experience with fast imaging. *Acta Radiol. Suppl.* **1986**, *369*, 561−563.
(8) Girardot, C.; Boukobza, M.; Lamoureux, J. P.; Sichez, J. P.; Capelle, L.; Zouaoui, A.; Bencherif, B.; Metzger, J. Choroid plexus papillomas of the posterior fossa in adults: MR imaging and gadolinium enhancement. Report of four cases and review of the literature. *J. Neuroradiol.* **1990**, *17*, 303−318.
(9) Rogosnitzky, M.; Branch, S. Gadolinium-based contrast agent toxicity: a review of known and proposed mechanisms. *BioMetals* **2016**, *29*, 365−76.
(10) Sieber, M. A.; Steger-Hartmann, T.; Lengsfeld, P.; Pietsch, H. Gadolinium-based contrast agents and NSF: evidence from animal experience. *J. Magn. Reson. Imaging* **2009**, *30*, 1268−1276.
(11) Prince, M. R.; Zhang, H. L.; Prowda, J. C.; Grossman, M. E.; Silvers, D. N. Nephrogenic systemic fibrosis and its impact on abdominal imaging. *Radiographics* **2009**, *29*, 1565−1574.
(12) Idée, J. M.; Port, M.; Dencausse, A.; Lancelot, E.; Corot, C. Involvement of gadolinium chelates in the mechanism of nephrogenic systemic fibrosis: an update. *Radiol. Clin. North Am.* **2009**, *47*, 855−869.
(13) Grobner, T. Gadolinium-a specific trigger for the development of nephrogenic fibrosing dermopathy and nephrogenic systemic fibrosis? *Nephrol., Dial., Transplant.* **2006**, *21*, 1104−1108.
(14) Marckmann, P.; Skov, L.; Rossen, K.; Dupont, A.; Damholt, M. B.; Heaf, J. G.; Thomsen, H. S. Nephrogenic systemic fibrosis: suspected causative role of gadodiamide used for contrast-enhanced magnetic resonance imaging. *J. Am. Soc. Nephrol.* **2006**, *17*, 2359−2362.
(15) http://www.ema.europa.eu/docs/en_GB/document_library/Referrals_document/gadolinium_contrast_agents_31/Recommendation_provided_by_Pharmacovigilance_Risk_Assessment_Committee/WC500223161.pdf.
(16) Laurent, S.; Forge, D.; Port, M.; Roch, A.; Robic, C.; Van der Elst, L.; Muller, R. N. Magnetic iron oxide nanoparticles: synthesis, stabilization, vectorization, physicochemical characterizations, and biological applications. *Chem. Rev.* **2008**, *108*, 2064−2110.
(17) Piloni, A.; Simonutti, R.; Stenzel, M. H. The effect of cationic groups on the stability of ^{19}F mri contrast agents in nanoparticles. *J. Polym. Sci., Part A: Polym. Chem.* **2019**, *57*, 1994−2001.
(18) Addisu, K. D.; Hailemeskel, B. Z.; Mekuria, S. L.; Andrgie, A. T.; Lin, Y. C.; Tsai, H. C. Bioinspired, Manganese-Chelated Alginate-Polydopamine Nanomaterials for Efficient in Vivo T1-Weighted Magnetic Resonance Imaging. *ACS Appl. Mater. Interfaces* **2018**, *10*, 5147−5160.
(19) Caillé, J. M.; Lemanceau, B.; Bonnemain, B. Gadolinium as a contrast agent for NMR. *Magn. Reson. Imaging* **1984**, *2*, 149.
(20) Pan, D.; Schmieder, A. H.; Wickline, S. A.; Lanza, G. M. Manganese-based MRI contrast agents: past, present and future. *Tetrahedron* **2011**, *67*, 8431−8444.
(21) Jørgensen, J. T.; Rief, M.; Brismar, T. B.; Wagner, M.; Albiin, N. A new manganese-based oral contrast agent (CMC-001) for liver MRI: pharmacological and pharmaceutical aspects. *Acta Radiol.* **2012**, *53*, 707−713.
(22) Gee, M. S.; Harisinghani, M. G. MRI in patients with inflammatory bowel disease. *J. Magn. Reson. Imaging* **2011**, *33*, 527−534.
(23) Bertin, A.; Steibel, J.; Michou-Gallani, A. I.; Gallani, J. L.; Felder-Flesch, D. Development of a dendritic manganese-enhanced magnetic resonance imaging (MEMRI) contrast agent: synthesis, toxicity (in vitro) and relaxivity (in vitro, in vivo) studies. *Bioconjugate Chem.* **2009**, *20*, 760−767.
(24) Gilad, A. A.; Walczak, P.; McMahon, M. T.; Na, H. B.; Lee, J. H.; An, K.; Hyeon, T.; van Zijl, P. C.; Bulte, J. W. MR tracking of transplanted cells with "positive contrast" using manganese oxide nanoparticles. *Magn. Reson. Med.* **2008**, *60*, 1−7.
(25) Pan, D.; Senpan, A.; Caruthers, S. D.; Williams, T. A.; Scott, M. J.; Gaffney, P. J.; Wickline, S. A.; Lanza, G. M. Sensitive and efficient detection of thrombus with fibrin-specific manganese nanocolloids. *Chem. Commun.* **2009**, *22*, 3234−3236.
(26) Zhen, Z.; Xie, J. Development of manganese-based nanoparticles as contrast probes for magnetic resonance imaging. *Theranostics* **2012**, *2*, 45−54.
(27) Qin, L.; Sun, Z. Y.; Cheng, K.; Liu, S. W.; Pang, J. X.; Xia, L. M.; Chen, W. H.; Cheng, Z.; Chen, J. X. Zwitterionic manganese and gadolinium metal-organic frameworks as efficient contrast agents for in vivo magnetic resonance imaging. *ACS Appl. Mater. Interfaces* **2017**, *9*, 41378−41386.
(28) Na, H. B.; Lee, J. H.; An, K.; Park, Y. I.; Park, M.; Lee, I. S.; Nam, D. H.; Kim, S. T.; Kim, S. H.; Kim, S. W.; Lim, K. H.; Kim, K. S.; Kim, S. O.; Hyeon, T. Development of a T_1 contrast agent for magnetic resonance imaging using MnO nanoparticles. *Angew. Chem., Int. Ed.* **2007**, *46*, 5397−5401.
(29) Mertzman, J. E.; Kar, S.; Lofland, S.; Fleming, T.; Van Keuren, E.; Tong, Y. Y.; Stoll, S. L. Surface attached manganese-oxo clusters as potential contrast agents. *Chem. Commun.* **2009**, *7*, 788−790.
(30) Skjold, A.; Amundsen, B. H.; Wiseth, R.; Støylen, A.; Haraldseth, O.; Larsson, H. B.; Jynge, P. Manganese dipyridoxyl-diphosphate (MnDPDP) as a viability marker in patients with myocardial infarction. *J. Magn. Reson. Imaging.* **2007**, *26*, 720−727.
(31) http://www.ema.europa.eu/docs/en_GB/document_library/Public_statement/2012/08/WC500130495.pdf.
(32) http://mriquestions.com/mn-agents-teslascan.html.
(33) Wang, J.; Wang, H.; Ramsay, I. A.; Erstad, D. J.; Fuchs, B. C.; Tanabe, K. K.; Caravan, P.; Gale, E. M. Manganese-based contrast agents for magnetic resonance imaging of liver tumors: Structure−activity relationships and lead candidate evaluation. *J. Med. Chem.* **2018**, *61*, 8811−8824.
(34) Huang, C. C.; Khu, N. H.; Yeh, C. S. The characteristics of sub 10 nm manganese oxide T1 contrast agents of different nanostructured morphologies. *Biomaterials* **2010**, *31*, 4073−4078.
(35) Zhou, Z.; Yang, L.; Gao, J.; Chen, X. Structure−relaxivity relationships of magnetic nanoparticles for magnetic resonance imaging. *Adv. Mater.* **2019**, *31*, 1804567.
(36) Xie, J.; Liu, G.; Eden, H. S.; Ai, H.; Chen, X. Surface-engineered magnetic nanoparticle platforms for cancer imaging and therapy. *Acc. Chem. Res.* **2011**, *44*, 883−892.
(37) Bennewitz, M. F.; Lobo, T. L.; Nkansah, M. K.; Ulas, G.; Brudvig, G. W.; Shapiro, E. M. Biocompatible and pH-sensitive PLGA encapsulated MnO nanocrystals for molecular and cellular MRI. *ACS Nano* **2011**, *5*, 3438−3446.
(38) Koenig, S. H.; Brown, R. D., 3rd; Kurland, R.; Ohkit, S. Relaxivity and binding of Mn^{2+} ions in solutions of phosphatidylserine vesicles. *Magn. Reson. Med.* **1988**, *7*, 133−142.
(39) Zhao, Z.; Bao, J.; Fu, C.; Lei, M.; Cheng, J. Controllable synthesis of manganese oxide nanostructures from 0-d to 3-d and mechanistic investigation of internal relation between structure and t1 relaxivity. *Chem. Mater.* **2017**, *29*, 10455−10468.
(40) Zhao, Z.; Fan, H.; Zhou, G.; Bai, H.; Liang, H.; Wang, R.; Zhang, X.; Tan, W. Activatable fluorescence/MRI bimodal platform

https://dx.doi.org/10.1021/acsanm.0c00474
ACS Appl. Nano Mater. 2020, 3, 3787−3797

for tumor cell imaging via mno2 nanosheet−aptamer nanoprobe. *J. Am. Chem. Soc.* **2014**, *136*, 11220−11223.
(41) Tawfilas, M.; Mauri, M.; De Trizio, L.; Lorenzi, R.; Simonutti, R. Surface characterization of TiO_2 polymorphic nanocrystals through ^1H TD-NMR. *Langmuir* **2018**, *34*, 9460−9469.
(42) Rowe, M. D.; Chang, C. C.; Thamm, D. H.; Kraft, S. L.; Harmon, J. F., Jr.; Vogt, A. P.; Sumerlin, B. S.; Boyes, S. G. Tuning the magnetic resonance imaging properties of positive contrast agent nanoparticles by surface modification with raft polymers. *Langmuir* **2009**, *25*, 9487−9499.
(43) Truffi, M.; Colombo, M.; Peñaranda-Avila, J.; Sorrentino, L.; Colombo, F.; Monieri, M.; Collico, V.; Zerbi, P.; Longhi, E.; Allevi, R.; Prosperi, D.; Corsi, F. Nano-targeting of mucosal addressin cell adhesion molecule-1 identifies bowel inflammation foci in murine model. *Nanomedicine* **2017**, *12*, 1547−1560.
(44) Colombo, M.; Fiandra, L.; Alessio, G.; Mazzucchelli, S.; Nebuloni, M.; De Palma, C.; Kantner, K.; Pelaz, B.; Rotem, R.; Corsi, F.; Parak, W. J.; Prosperi, D. Tumour homing and therapeutic effect of colloidal nanoparticles depend on the number of attached antibodies. *Nat. Commun.* **2016**, *7*, 13818.
(45) Song, C. X.; Labhasetwar, V.; Murphy, H.; Qu, X.; Humphrey, W. R.; Shebuski, R. J.; Levy, R. J. Formulation and characterization of biodegradable nanoparticles for intravascular local drug delivery. *J. Controlled Release* **1997**, *43*, 197−212.
(46) Kumar, V.; Singh, K.; Panwar, S.; Mehta, S. K. Green synthesis of manganese oxide nanoparticles for the electrochemical sensing of p-nitrophenol. *Int. Nano Lett.* **2017**, *7*, 123−131.
(47) Vismara, E.; Bongio, C.; Coletti, A.; Edelman, R.; Serafini, A.; Mauri, M.; Simonutti, R.; Bertini, S.; Urso, E.; Assaraf, Y. G.; Livney, Y. D. Albumin and hyaluronic acid-coated superparamagnetic iron oxide nanoparticles loaded with paclitaxel for biomedical applications. *Molecules* **2017**, *22*, 1030.
(48) Huang, G.; Li, H.; Chen, J.; Zhao, Z.; Yang, L.; Chi, X.; Chen, Z.; Wang, X.; Gao, J. Tunable T_1 and T_2 contrast abilities of manganese-engineered iron oxide nanoparticles through size control. *Nanoscale* **2014**, *6*, 10404−10412.
(49) Gao, Z.; Ma, T.; Zhao, E.; Docter, D.; Yang, W.; Stauber, R. H.; Gao, M. Small is smarter: nano MRI contrast agents - advantages and recent achievements. *Small* **2016**, *12*, 556−576.
(50) Simon, G. H.; Bauer, J.; Saborovski, O.; Fu, Y.; Corot, C.; Wendland, M. F.; Daldrup-Link, H. E. T_1 and T_2 relaxivity of intracellular and extracellular USPIO at 1.5T and 3T clinical MR scanning. *Eur. Radiol.* **2006**, *16*, 738−745.
(51) Southon, T. E.; Grant, D.; Bjørnerud, A.; Moen, O. M.; Spilling, B.; Martinsen, I.; Refsum, H. NMR relaxation studies with MnDPDP. *Acta Radiol.* **1997**, *38*, 708−716.
(52) Giesel, F. L.; von Tengg-Kobligk, H.; Wilkinson, I. D.; Siegler, P.; von der Lieth, C. W.; Frank, M.; Lodemann, K. P.; Essig, M. Influence of human serum albumin on longitudinal and transverse relaxation rates (r_1 and r_2) of magnetic resonance contrast agents. *Invest. Radiol.* **2006**, *41*, 222−228.
(53) Caravan, P.; Farrar, C. T.; Frullano, L.; Uppal, R. Influence of molecular parameters and increasing magnetic field strength on relaxivity of gadolinium- and manganese-based T_1 contrast agents. *Contrast Media Mol. Imaging* **2009**, *4*, 89−100.
(54) Selli, D.; Tawfilas, M.; Mauri, M.; Simonutti, R.; Di Valentin, C. Optimizing pegylation of TiO_2 nanocrystals through a combined experimental and computational study. *Chem. Mater.* **2019**, *31*, 7531−7546.
(55) Langer, G. A.; Serena, S. D.; Nudd, L. M. Localization of contractile-dependent Ca: comparison of Mn and verapamil in cardiac and skeletal muscle. *Am. J. Physiol.* **1975**, *229*, 1003−1007.
(56) Haworth, R. A.; Goknur, A. B.; Berkoff, H. A. Measurement of Ca channel activity of isolated adult rat heart cells using ^{54}Mn. *Arch. Biochem. Biophys.* **1989**, *268*, 594−604.
(57) Crossgrove, J.; Zheng, W. Manganese toxicity upon over-exposure. *NMR Biomed.* **2004**, *17*, 544−553.
(58) Wolf, G. L.; Baum, L. Cardiovascular toxicity and tissue proton T_1 response to manganese injection in the dog and rabbit. *AJR, Am. J. Roentgenol.* **1983**, *141*, 193−197.
(59) Gallez, B.; Bacic, G. G.; Swartz, H. M. Evidence for the dissociation of the hepatobiliary MRI contrast agent Mn-DPDP. *Magn. Reson. Med.* **1996**, *35*, 14−19.
(60) Federle, M. P.; Chezmar, J. L.; Rubin, D. L.; Weinreb, J. C.; Freeny, P. C.; Semelka, R. C.; Brown, J. J.; Borrello, J. A.; Lee, J. K.; Mattrey, R.; Dachman, A. H.; Saini, S.; Harmon, B.; Fenstermacher, M.; Pelsang, R. E.; Harms, S. E.; Mitchell, D. G.; Halford, H. H.; Anderson, M. W.; Johnson, C. D.; Francis, I. R.; Bova, J. G.; Kenney, P. J.; Klippenstein, D. L.; Foster, G. S.; Turner, D. A.; et al. Safety and efficacy of mangafodipir trisodium (MnDPDP) injection for hepatic MRI in adults: results of the U.S. multicenter phase III clinical trials (safety). *J. Magn. Reson. Imaging* **2000**, *12*, 186−197.

https://dx.doi.org/10.1021/acsanm.0c00474
ACS Appl. Nano Mater. 2020, 3, 3787−3797